Vibration modelling and verifications for whole aero-engine

G. Chen

College of Civil Aviation, Nanjing University of Aeronautics and Astronautics, Nanjing 210016, PR China

ARTICLE INFO

ABSTRACT

In this study, a new rotor–ball-bearing–casing coupling dynamic model for a practical aero-engine is established. In the coupling system, the rotor and casing systems are modelled using the finite element method, support systems are modelled as lumped parameter models, nonlinear factors of ball bearings and faults are included, and four types of supports and connection models are defined to model the complex rotor–support–casing coupling system of the aero-engine. A new numerical integral method that combines the Newmark-β method and the improved Newmark-β method (Zhai method) is used to obtain the system responses. Finally, the new model is verified in three ways: (1) modal experiment based on rotor–ball bearing rig, (2) modal experiment based on rotor–ball-bearing–casing rig, and (3) fault simulations for a certain type of missile turbofan aero-engine vibration. The results show that the proposed model can not only simulate the natural vibration characteristics of the whole aero-engine but also effectively perform nonlinear dynamic simulations of a whole aero-engine with faults.

1. Introduction

In general, aero-engine rotors are supported on stator casings through ball bearings, and the casings are supported on a base. To reduce rotor vibrations and adjust the critical speeds of the system, flexible supports are usually designed between the outer race and the housing of the bearings. The motions of the rotors, bearings, and casings are affected by each other. Consequently, the rotor–support–casing coupling system is investigated from the viewpoint of structure and dynamics [1].

Thus far, many studies have investigated the vibration characteristics of an aero-engine. Ou [2] analysed the whole aero-engine vibration characteristics of the rotor–support–casing system by combining a modal synthesis method and a finite element method. Chen [3] studied the dynamics characteristics of the whole aero-engine using NASTRAN software and found a coupling vibration between the rotor's higher-order bending vibration modes and casing vibration; finally, methods for determining the rotor system's critical speeds were studied by considering the casing vibration. Hong [4] computed the dynamics characteristics of a certain type of engine using the static stiffness, dynamic stiffness, and a whole aero-engine finite element model; they indicated that a whole aero-engine model can be used to analyse the effect of the support dynamic stiffness and local casing vibration on the whole aero-engine. Chiang [5] studied the vibration characteristics of a single/dual rotor–ball bearing system using the finite element method. Sun [6] proposed a flexible dual-rotor finite element model based on a detailed nonlinear characteristics consideration for ball bearings and the squeeze film damper and stimulated the transient responses of the blade loss. Sun [7] proposed a dual-rotor gas turbine engine finite element model and used a numerical integration method to calculate the sudden unbalance response under blade loss; in doing so, they considered the contact nonlinearity of a ball bearing, nonlinearity of the squeeze film force, and thermal increase effect of bearing components during blade loss. Hai and Bonello [8] established a dual rotor-rolling bearing system with a nonlinear squeeze film damper; they conducted nonlinear numerical simulations by combining NASTRAN finite element software with MATLAB and showed that the computing speed was greatly improved.

E-mail address: cgzyx@263.net

In a rotor–support–casing coupling system, there are many nonlinear factors such as the clearance, nonlinear contact force, varying compliance (VC) vibration of ball bearing, and nonlinear oil-film force of squeeze film damper (SFD). In particular, when rotor and bearing faults such as rubbing, looseness, misalignment, and bearing damage occur, the rotor–support–casing coupling system shows stronger nonlinear characteristics. However, nonlinear dynamic problems are very difficult to solve using the traditional transfer matrix method, modal synthesis method, finite element method, and impedance coupling method. Chen [9] proposed a new rotor–ball-bearing-casing coupling dynamic model in which the nonlinear factors of the bearing, SFD, and rubbing fault are considered, and the rotor is considered a free Euler beam model with an equal section. The numerical integral method is used to obtain the system's responses, and the whole aero-engine vibrations and characteristics of rub-impact are analysed; however, it is difficult to analyse a rotor with a variable cross section using this method.

Therefore, the modern aero-engine structure is very complex, and it is very difficult to establish a detailed whole aero-engine finite element model because a computer can barely handle the large computational load required for the same. In addition, it is very difficult to solve complex nonlinear responses. In this light, to solve the whole aero-engine vibration, a new rotor–support–casing nonlinear coupling dynamic model is proposed in this study. In the proposed model, the rotor and casing systems are modelled using the finite element method; support systems are modelled by lumped parameter models; nonlinear factors of ball bearings and all types of faults are included; and four types of supports and connection modes are defined to model the complex rotor–support–casing coupling system. A new numerical integral method that combines the Newmark-β method and the improved Newmark-β method (Zhai method) is used to obtain the system responses. Finally, the new model is verified in three ways.

2. Aero-engine rotor–support–casing coupling dynamic model

The aero-engine rotor–support–casing coupling dynamic model consists of the rotors, supports, and casings. The finite element method is used to establish the model of the rotors and casings, and the discrete lumped mass model is used to model all types of supports. The coupling between parts is enabled by the action and the reaction forces. Finally, the numerical integral method is used to solve the differential equation of motion. The rotors, casings, and supports (connections) in the coupling system are modelled as follows.

2.1. Rotor model

The rotor consists of a number of rigid rotating discs and an elastic shaft. The former is modelled as a discrete lumped mass, and its mass, inertia, and gyroscopic moments are considered. The latter is discretised using a beam element model, and its shear deformations, gyroscopic moments, and inertia are considered. All parts are coupled by nonlinear forces and moments. Fig. 1 shows the finite element rotor dynamic model.

For each rotor shaft beam element, E, I, G, μ, L, ρ, and A respectively denote the elastic modulus, moment of inertia, shear modulus, Poisson's ratio, shaft length, shaft density, and shaft cross-sectional area. P_i is the rigid rotating disc; F_{xi}, F_{yi}, M_{xi}, and M_{yi} are forces and moments that act on the ith node of the rotor in the X and Y directions. Fig. 3 shows the *O-XYZ* fixed coordinate system. Under a deformation state, any cross section's position relative to the fixed coordinate system is determined as follows: elastic shaft centerline position is determined by the displacement x in the X direction and the displacement y in the Y direction, cross-sectional orientation ϕ is determined by the angle around the X axis and the angle ψ around the Y axis, and the cross section also rotates around the Z axis.

(1) **Motion equations of rigid disc element**

Suppose the rigid disc's mass is m^d, rotor cross-equator inertia is J_d^d, cross-polar inertia is J_p^d, and ω is the rotating speed of the disc. Through the Lagrange equation, we can obtain the motion equations of the rigid disc relative to the fixed coordinate system.

$$(\mathbf{M}_T^d + \mathbf{M}_R^d)\ddot{\mathbf{q}}^d - \omega \mathbf{G}^d \dot{\mathbf{q}}^d = \mathbf{Q}^d \tag{1}$$

where $\mathbf{Q}^d$ is the generalised external force vector; $\mathbf{M}_T^d$ and $\mathbf{M}_R^d$ are respectively the mass matrix and mass inertia matrix;
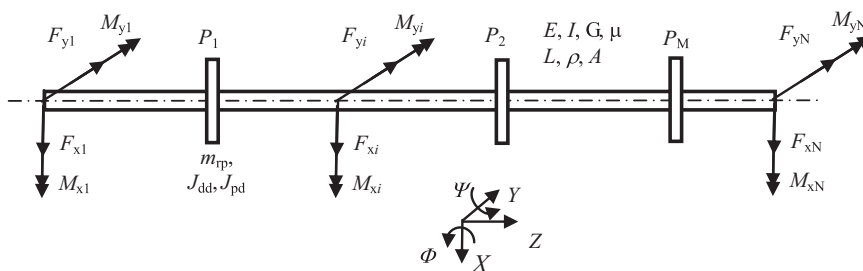

Fig. 1. Finite element rotor dynamic model.

$\mathbf{G}^d$ is the gyroscopic matrix; and $\mathbf{q}$ is the generalised displacement vector, where $\mathbf{q} = [x, y, \phi, \psi]$. Then,

$$\mathbf{M}_T^d = \begin{bmatrix} m^d & 0 & 0 & 0 \\ 0 & m^d & 0 & 0 \\ 0 & 0 & 0 & 0 \\ 0 & 0 & 0 & 0 \end{bmatrix}, \quad \mathbf{M}_R^d = \begin{bmatrix} 0 & 0 & 0 & 0 \\ 0 & 0 & 0 & 0 \\ 0 & 0 & J_d^d & 0 \\ 0 & 0 & 0 & J_d^d \end{bmatrix}, \quad \mathbf{G}^d = \begin{bmatrix} 0 & 0 & 0 & 0 \\ 0 & 0 & 0 & 0 \\ 0 & 0 & 0 & -J_p^d \\ 0 & 0 & J_p^d & 0 \end{bmatrix}$$

(2) **Motion equations of beam element**

In this study, beam elements are adopted. Each beam element has two nodes and eight DOFs. Each node has four DOFs, which are respectively the displacements x and y in the X and Y directions, and rotating angles ϕ and ψ around the X and Y axes. The cross section's displacement of the element is a function of the time and position along the element axis. The generalised displacement vector of the element is $\mathbf{q}^e(t) = \begin{bmatrix} q_1^e & q_2^e & q_3^e & q_4^e & q_5^e & q_6^e & q_7^e & q_8^e \end{bmatrix}^{\mathrm{T}}$. Through the Lagrange equation, the motion equations of the beam element relative to the fixed coordinate system can be obtained.

$$(\mathbf{M}_T^e + \mathbf{M}_R^e)\ddot{\mathbf{q}}^e + (-\omega\mathbf{G}^e)\dot{\mathbf{q}}^e + (\mathbf{K}_B^e - \mathbf{K}_A^e)\mathbf{q}^e = \mathbf{Q}^e \tag{2}$$

where $\mathbf{Q}^e$ is the generalised external force vector; $\mathbf{M}_T^e$ and $\mathbf{M}_R^e$ are respectively the mass matrix and mass inertia matrix; $\mathbf{G}^e$ is the gyroscopic matrix; $\mathbf{K}_B^e$ is the element's bending and shear stiffness matrix; and $\mathbf{K}_A^e$ is the element's tensile stiffness matrix. These matrixes have been described in literature [1,10].

The rotor system's motion equation through the element's motion equations can be obtained as follows:

$$(\mathbf{M}^s)\ddot{\mathbf{q}}^s + (\mathbf{C}^s - \omega\mathbf{G}^s)\dot{\mathbf{q}}^s + \mathbf{K}^s\mathbf{q}^s = \mathbf{Q}^s \tag{3}$$

where $\mathbf{Q}^s$ is the generalised external force vector; $\mathbf{M}^s$, the mass matrix; $\mathbf{G}^s$, the gyroscopic matrix; $\mathbf{K}^s$, the system's stiffness matrix; and $\mathbf{C}^s$, the system's damping matrix.

In this study, $\mathbf{C}^s$ is assumed to be the proportional damping matrix, that is, $\mathbf{C}^s = \alpha_0\mathbf{M}^s + \alpha_1\mathbf{K}^s$, where α_0 and α_1 are constants. The ith order damping ratio is

$$\xi_i = \frac{1}{2}\left(\frac{\alpha_0}{\omega_i} + \alpha_1\omega_i\right) \tag{4}$$

Obviously, after any two natural frequencies and damping ratios of the rotor are obtained through a modal experiment, α_0 and α_1 can be solved through Eq. (4), and the system's damping ratio matrix $\mathbf{C}^s$ can be obtained.

2.2. Casing model

In general, the casing finite element model can be constructed by the beam element, conical shell element, and surface shell element. The casing is a shell structure, and its vibration mode has many forms whose circumferential wave number is 0, 1, 2, …, and so on. However, when the casing couples with the rotor, only the mode of wave number 1 appears, and the cross section of the rotor does not deform. Therefore, the casing can be constructed using a common beam element that does not rotate [1].

In this study, the casing is modelled as a beam that does not rotate, as in rotor modelling. By a finite element modelling method, the differential equation of motion of the casing is

$$(\mathbf{M}^c)\ddot{\mathbf{q}}^c + \mathbf{C}^c\dot{\mathbf{q}}^c + \mathbf{K}^c\mathbf{q}^c = \mathbf{Q}^c \tag{5}$$

where $\mathbf{Q}^c$ is the generalised excitation force vector; $\mathbf{M}^c$, the mass matrix of the casing; $\mathbf{K}^c$, the stiffness matrix of the casing; $\mathbf{C}^c$, the damper matrix of the casing; and $\mathbf{C}^s$, the proportional damping matrix.

2.3. Discrete support model

To model a practical complex aero-engine with multiple rotors and casings, the connection relationship among the rotor, casing, and support needs to be considered in detail. Therefore, in this study, four types of connection forms are defined: support connection between rotor and casing, shaft coupling connection between rotor and rotor, elastic connection between casing and casing, and installation connection between casing and base. By synthetically using these four types of connections, the whole aero-engine with multiple rotors and casings can be modelled very conveniently.

(1) **Support connection between rotor and casing**

Each support connection between the rotor and the casing RC_i ($i=1, 2, …, N$), includes a ball bearing and bearing housing. Suppose that m_{wi} is the outer mass of the bearing; m_{bi} is the mass of the bearing housing; k_{ti} is the support stiffness between the outer race and the bearing house; c_{ti} is the damping coefficient between the outer race and the bearing housing; k_{fi} and c_{fi} are respectively the support stiffness and damping coefficient between the casing and the bearing housing. As shown in Fig. 2, F_{yRi} and F_{xRi} are the rotor force acting on the support RC_i, and F_{yCi} and F_{xCi} are the casing force acting on the support RC_i. It is assumed that the support RC_i is connected with the mth node of the rotor and the nth node of the casing.
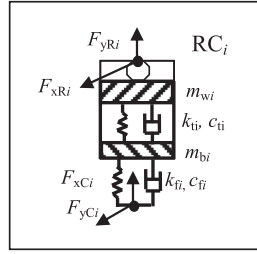
Fig. 2. Rotor–casing support.

Generally, in aero-engine design, an elastic support with stiffness k_{ti} is installed between the bearing outer ring and the bearing house. The stiffness of the elastic support can be computed according to its structure type or be measured experimentally. k_{fi} is the stiffness between the bearing house and the casing, and it can be simplified as a cylindrical model with one end fixed and the other end free according to the connection characteristics; the stiffness can be computed by the finite element method. In this study, the bearing outer ring is supposed to be connected to the bearing housing and does not rotate; the inner ring is fixed on the rotating shaft. Assume that the displacements of the mth node of the rotor are x_{Rm} and y_{Rm}. Let $x = x_{Rm} - x_{wi}$, $y = y_{Rm} - y_{wi}$. According to the literature [11,12], the ball force can be expressed as

$$\begin{cases} F_{xRi} = \sum_{j=1}^{N} C_b(x \cos \theta_j + y \sin \theta_j - r_0)^{3/2} H(x \cos \theta_j + y \sin \theta_j - r_0) \cos \theta_j \\ F_{yRi} = \sum_{j=1}^{N} C_b(x \cos \theta_j + y \sin \theta_j - r_0)^{3/2} H(x \cos \theta_j + y \sin \theta_j - r_0) \sin \theta_j \end{cases} \tag{6}$$

In this equation, C_b is the Hertzian contact stiffness, and it can be obtained from the nonlinear Hertzian contact elastic analysis of the inner race, outer race, and balls. $H(\bullet)$ is the Heaviside function; when the function's independent variable is greater than 0, the function value is 1; otherwise, it is 0. θ_j is the jth ball's angle position, that is, $\theta_j = \omega_{Cage} \times t + \frac{2\pi}{N_b}(j-1)$, $j = 1, 2, \cdots N_b$, where N_b is the number of balls. ω_{Cage} is the rotating speed of the cage. Suppose that the outer race radius is R, inner ring radius is r, $\omega_{Cage} = \frac{\omega \times r}{R+r}$, and ω is the shaft rotating angular velocity.

Therefore, the bearing outer race's differential equation of motion is

$$\begin{cases} m_{wi}\ddot{x}_{wi} + k_{ti}(x_{wi} - x_{bi}) + F_{dxi} = F_{xRi} \\ m_{wi}\ddot{y}_{wi} + k_{ti}(y_{wi} - y_{bi}) + F_{dyi} = F_{yRi} - m_{wi}g \end{cases} \quad i = 1, 2, \cdots N \tag{7}$$

here F_{dxi} and F_{dyi} are damping forces. If the viscous damping is considered, then

$$F_{dxi} = c_{ti}(\dot{x}_{wi} - \dot{x}_{bi}), \quad F_{dyi} = c_{ti}(\dot{y}_{wi} - \dot{y}_{bi}) \tag{8}$$

Otherwise, the damping forces would be nonlinear, such as the damping forces arising from the SFDs and other nonlinear dampers.

(2) **Coupling connection between rotor and rotor**

Assume that the coupling connect RRC_k ($k = 1, 2, \ldots, N$) connects the ith node of the left rotor and the jth node of the right rotor. The radial stiffness of coupling is k_{Rr}, angular stiffness is $k_{R\alpha}$, radial damping is c_{Rr}, and angular damping is $c_{R\alpha}$. The generalised displacements of the ith node of the left rotor are $x_{RLi}, y_{RLi}, \phi_{RLi}, \psi_{RLi}$, velocities are $\dot{x}_{RLi}, \dot{y}_{RLi}, \dot{\phi}_{RLi}, \dot{\psi}_{RLi}$; jth node displacements of the right rotor are $x_{RRj}, y_{RRj}, \phi_{RRj}, \psi_{RRj}$, and velocities are $\dot{x}_{RRj}, \dot{y}_{RRj}, \dot{\phi}_{RRj}, \dot{\psi}_{RRj}$. Then, the forces and moments that act on the ith node of the left rotor, $F_{Rxi}, F_{Ryi}, M_{Rxi}$, and M_{Ryi}, and the forces and moments for the jth node of the right rotor, $F_{Rxj}, F_{Ryj}, M_{Rxj}$, and M_{Ryj} are

$$\begin{cases} F_{Rxi} = k_{Rr}(x_{RRj} - x_{RLi}) + c_{Rr}(\dot{x}_{RRj} - \dot{x}_{RLi}) \\ F_{Ryi} = k_{Rr}(y_{RRj} - y_{RLi}) + c_{Rr}(\dot{y}_{RRj} - \dot{y}_{RLi}) \\ M_{Rxi} = k_{R\alpha}(\phi_{RRj} - \phi_{RLi}) + c_{R\alpha}(\dot{\phi}_{RRj} - \dot{\phi}_{RLi}) \\ M_{Ryi} = k_{R\alpha}(\psi_{RRj} - \psi_{RLi}) + c_{R\alpha}(\dot{\psi}_{RRj} - \dot{\psi}_{RLi}) \end{cases} \quad \begin{cases} F_{Rxj} = -F_{Rxi} \\ F_{Ryj} = -F_{Ryi} \\ M_{Rxj} = -M_{Rxi} \\ M_{Ryj} = -M_{Ryi} \end{cases} \tag{9}$$

In general, the types of coupling include gear coupling, diaphragm coupling, and flange bolt coupling. The coupling's radial stiffness k_{Rr} and angular stiffness $k_{R\alpha}$ can be computed according to its type and structure, and they can also be measured experimentally.

(3) **Elastic connection between casing and casing**

The elastic connection between the casing and the casing CC_k ($k = 1, 2, \ldots, N$) connects the ith node of casing 1 and jth node of casing 2. The radial stiffness, angular stiffness, radial damping, and angular damping are respectively $k_{Cr}, k_{C\alpha}, c_{Cr}$,

and $c_{C\alpha}$. The generalised displacements of the ith node of casing 1 are x_{C1i}, y_{C1i}, ϕ_{C1i}, ψ_{C1i}, velocities are $\dot{x}_{C1i}$, $\dot{y}_{C1i}$, $\dot{\phi}_{C1i}$, $\dot{\psi}_{C1i}$; generalised displacements of the jth node of casing 2 are x_{C2j}, y_{C2j}, ϕ_{C2j}, ψ_{C2j}, and velocities are $\dot{x}_{C2j}$, $\dot{y}_{C2j}$, $\dot{\phi}_{C2j}$, $\dot{\psi}_{C2j}$. The forces and moments acting on the ith node of casing 1 are F_{xi}, F_{yi}, M_{xi}, and M_{yi}, and the forces and moments acting on the jth node of casing 2 are F_{xj}, F_{yj}, M_{xj}, and M_{yj}. They are given as

$$\begin{cases} F_{C1xi} = k_{Cr}(x_{C2j}-x_{C1i})+c_{Cr}(\dot{x}_{C2j}-\dot{x}_{C1i}) \\ F_{C1yi} = k_{Cr}(y_{C2j}-y_{C1i})+c_{Cr}(\dot{y}_{C2j}-\dot{y}_{C1i}) \\ M_{C1xi} = k_{C\alpha}(\phi_{C2j}-\phi_{C1i})+c_{C\alpha}(\dot{\phi}_{C2j}-\dot{\phi}_{C1i}) \\ M_{C1yi} = k_{C\alpha}(\psi_{C2j}-\psi_{C1i})+c_{C\alpha}(\dot{\psi}_{C2j}-\dot{\psi}_{C1i}) \end{cases} \quad \begin{cases} F_{C2xj} = -F_{C1xi} \\ F_{C2yj} = -F_{C1yi} \\ M_{C2xj} = -M_{C1xi} \\ M_{C2yj} = -M_{C1yi} \end{cases} \quad (10)$$

Usually, the casings are connected to each other by bolts, and the bolts' connection stiffness k_{Cr} and $k_{C\alpha}$ can be computed using the finite element method and measured experimentally.

(4) **Elastic support (installation node) between casing and base**

The elastic connection between the casing and the base CB_k ($k=1, 2, …, N$) connects the ith node of the casing and the base. The support stiffness is k_C, and damping is c_C. The displacements of the ith node of the casing are x_{Ci}, y_{Ci}, and the velocities are $\dot{x}_{Ci}$, $\dot{y}_{Ci}$. Then, the forces acting on the ith node of the casing F_{Cxi} and F_{Cyi} are

$$\begin{cases} F_{Cxi} = -k_C x_{Ci} - c_C \dot{x}_{Ci} \\ F_{Cyi} = -k_C y_{Ci} - c_C \dot{y}_{Ci} \end{cases} \quad (11)$$

Here, the support stiffness k_C between the casing and the base can be computed using the finite element method or measured experimentally.

2.4. Solution of finite element rotor–support–casing coupling dynamic model

Because the number of DOFs in the finite element rotor–support–casing coupling dynamic model is very large and there are many strong nonlinear factors, in this study, a combination time integration approach is used to solve the system's responses, which combines the implicit Newmark-β method and the improved explicit Newmark-β method (Zhai method [13]). This finite element rotor–support coupling dynamic solution procedure is shown in Fig. 3.

The merits of the combination method are as follows: (1) the Newmark-β method is used to solve the rotor and casing finite element model and the Zhai method is used to solve the lumped parameter support models, making the combination method very suitable for solving a coupling system; and (2) an enormous matrix need not be formed and the matrixes of the rotors and the casings need not be combined into a large matrix, thus improving the computational efficiency greatly.

3. Model verification based on rotor tester

3.1. Verification based on rotor–ball-bearing tester

A rotor–ball-bearing fault tester (Shenyang Aero-engine Institute) can effectively simulate common faults in aero-engine rotors and ball bearings. The tester and dynamic model are shown in Fig. 4.

The rotor–ball-bearing fault tester includes a rotating shaft, a rotating disc, a flanged disc, two supports, a motor, and a gear-box. In the dynamic model, P_1 and P_2 are discs. P_1 is the rotor disc, and P_2 is the flanged disc connected with the gear output shaft. S_1 and S_2 are two supports. L_1, L_2, L_3, and L_4 decide each parts' position at the shaft. All model parameters need to be modified by experimental verification, and the experimental and simulation results ultimately show good consistency.
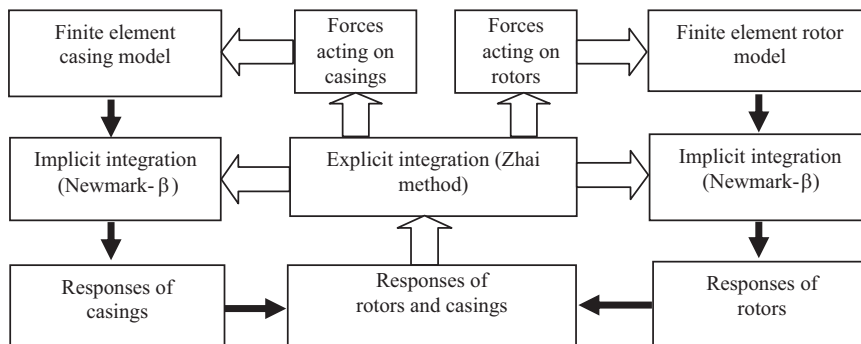

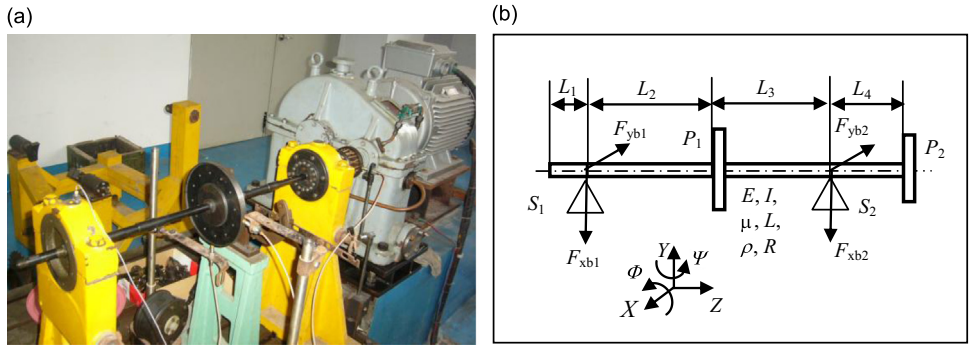**Fig. 3.** Solving flow for rotor–support–casing coupling dynamics.

Fig. 4. Rotor–ball-bearing tester and its dynamic model: (a) rotor–ball-bearing tester and (b) structure sketch map of tester.

Table 1
Rotor parameters of rotor–ball-bearing test rig.

Elastic modulus E (Pa)			Axis diameter D (m)	Density ρ (kg/m³)		Poisson's ratio μ	Proportion damping ratio α_0	Proportion damping ratio α_1
2.1×10^{11}			0.019	7.8×10^3		0.3	5	1.35×10^{-5}
L1 (mm)	L2 (mm)	L3 (mm)	Disc P_1 mass m_p (kg)	Disc P_1 polar moment of inertia J_{dp1} (kg m²)	Disc P_1 equatorial moment of inertia J_{dd1} (kg m²)	Disc P_2 mass m_{p2} (kg)	Disc P_2 polar moment of inertia J_{dp2} (kg m²)	Disc P_2 equatorial moment of inertia J_{dd2} (kg m²)
100	342	370	2.4	0.0125	0.00625	0.45	0.00025	0.000125

Table 2
Parameters of ball bearings.

Pitch diameter D_m (mm)	Ball diameter d (mm)	Outer raceway radius R (mm)	Inner raceway radius r (mm)	Ball number N_b	Contact stiffness C_b (N/m³/²)	Bearing clearance r_0 (μm)	Outer mass m_w (kg)	Bearing carrier mass m_w (kg)
36	9.6	22.8	13.2	7	11.67×10^9	0	0.08	76

Table 3
Parameters of supports.

k_t (N/m)	c_t (N s/m)	k_f (N/m)	c_f (N s/m)
1.0×10^8	500	3.0×10^7	2000

In this study, the modal analysis of the tester is performed by the hammer hitting method in the support state. The main equipment used includes an NI9234 dynamic signal acquisition module (NI Corporation), a 30927-type hammer (ENDEVCO Corporation), and a 4805-type ICP acceleration sensor (B&K Company). The experiment considers a single measuring point and many exciting points. The rotor–support coupling dynamic model is established, and by adjusting the parameters of the simulation model, the modal parameters of the simulation model and experimental model ultimately show good consistency. The final model dynamics parameters are obtained. The rotor parameters are listed in Table 1; the ball bearing parameters, in Table 2; and the support parameters, in Table 3.

Fig. 5 shows the amplitudes and phases of the original point frequency response functions (FRFs) obtained by calculation and experimental modal analysis. Table 4 shows a comparison between the calculated and the experimental modal parameters. Fig. 6 shows a comparison of the modes for the first four modal shapes. In the comparison of mode shapes, because the shaft is only hit from S1 to S2 in the experimental modal analysis, the mode shapes of the experimental mode include only the part between the dotted lines; however, in the calculation of the modal analysis, the vibration mode can be calculated from the far left to the far right of the shaft. Therefore, the vibration mode shape includes all parts inside and outside the dotted line in Fig. 6.

From Figs. 5 and 6, and Table 4, it can be concluded that the simulation results agree well with the experimental values. This proves that the proposed finite element rotor–support coupling system dynamics model is effective.
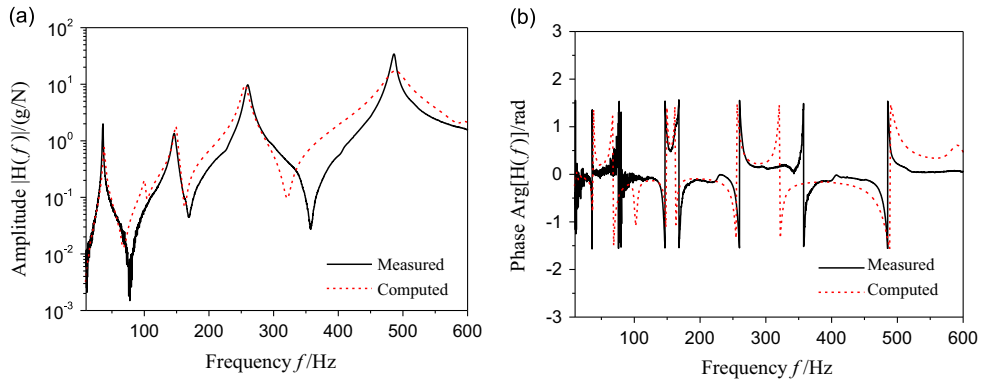
Fig. 5. Original point acceleration FRFs contrast between calculation and experimental modal analysis: (a) amplitude-frequency plot contrast and (b) phase-frequency plot contrast.

Table 4
Modal parameters from calculation and experiment.

Order	Experimental results		Simulation results	
	Natural frequency (Hz)	Damping ratio	Natural Frequency (Hz)	Damping ratio
1st	35.75	0.0116	37.81	0.0327
2nd	146.38	0.0173	148.86	0.0164
3rd	260.20	0.0133	255.80	0.0178
4th	485.79	0.0078	488.12	0.0326
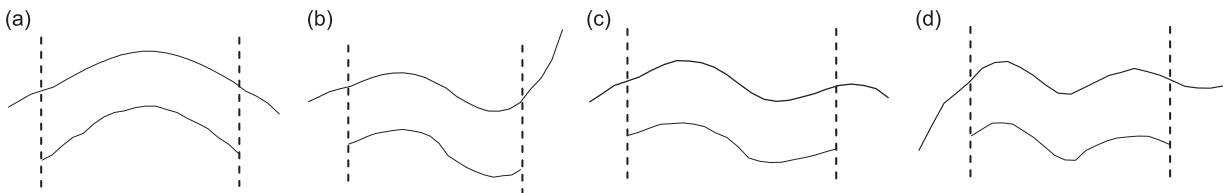
Fig. 6. Contrast between calculated and experimental modal shapes for first four orders: (a) 1st order; (b) 2nd order; (c) 3rd order; and (d) 4th order.
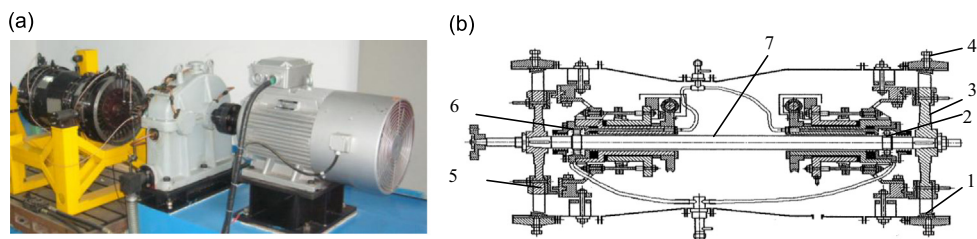
Fig. 7. Aero-engine rotor tester: (a) aero-engine rotor tester and (b) section drawing of aero-engine rotor tester. 1 – rubbing ring, 2 – ball bearing, 3 – turbine disc, 4 – bolt for deforming rubbing ring, 5 – compressor disc, 6 – ball bearing, 7 – shaft.

3.2. Verification based on rotor–ball-bearing–casing tester

3.2.1. Rotor–ball-bearing–casing tester

To simulate the rotor vibration of a real aero-engine, an aero-engine rotor tester [11] is designed and manufactured (Shenyang Aero-engine Institute). Fig. 7(a) and (b) shows its full-scale photograph and its section drawing, respectively.

The structure sketch map of the aero-engine rotor tester is shown in Fig. 8. The rotor comprises three discs, where P1 denotes the flange plate; P2, the compressor disc; and P3, the turbine disc. The casing includes seven segments, namely, AB, BC, CD, DE, EF, FG, and GH. The casings are connected by bolts. The rotor is supported by two supports, RC1 and RC2. The basic sizes are labelled in Fig. 8, and other parameters are listed in Tables 5–9. The finite unit number of rotors is 34, and the finite unit number of casings is 29.
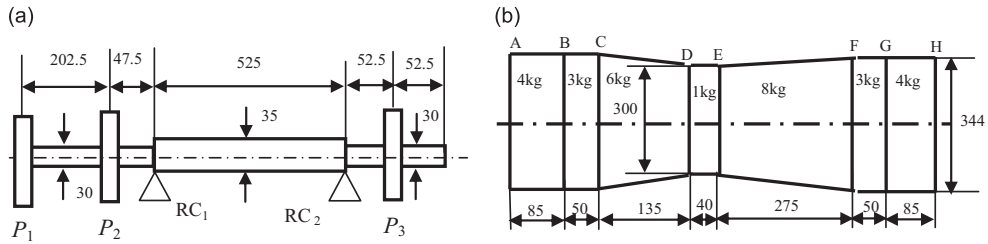
Fig. 8. Structure sketch map of aero-engine rotor tester (unit: mm): (a) rotor model (b) casing model.

Table 5
Main rotor parameters.

Parameters	Disc P_1	Disc P_2	Disc P_3
Mass m_p (kg)	0.5	10	10
Cross-polar inertia J_{dp} (kg m^2)	0.005	0.05	0.05
Cross-equator inertia J_{dd} (kg m^2)	0.0025	0.025	0.025
Elastic modulus E (Pa)	2.1×10^{11}	2.1×10^{11}	2.1×10^{11}
Poisson's ratio μ	0.3	0.3	0.3
Density ρ (kg/m^3)	7.8×10^3	7.8×10^3	7.8×10^3
Proportion damping ratio α_0	5	5	5
Proportion damping ratio α_1	1.35×10^{-5}	1.35×10^{-5}	1.35×10^{-5}

Table 6
Main parameters of casings.

Wall thickness (mm)						
AB	BC	CD	DE	EF	FG	GH
2	10	2	2	2	10	2

Elastic modulus E (Pa)	Density ρ (kg/m^3)	Poisson's ratio μ	Proportion damping ratio α_0	Proportion damping ratio α_1
2.1×10^{11}	7.8×10^3	0.3	5	1.35×10^{-5}

Table 7
Main parameters of ball bearing.

Pitch diameter D_m (mm)	Ball diameter d (mm)	Outer raceway radius R (mm)	Inner raceway radius r (mm)	Ball number N_b	Contact stiffness C_b (N/m$^{3/2}$)	Bearing clearance r_0 (μm)	Outer mass m_w (kg)	Bearing carrier mass m_w (kg)
36	9.6	22.8	13.2	7	11.67×10^9	0	0.08	10

Table 8
Support parameters of rotor–casing.

Supports	Node of rotor	Casing (node)	k_t (N/m)	c_t (N s/m)	k_f (N/m)	c_f (N s/m)
RC$_1$	11	6	6.0×10^6	1000	7.0×10^6	1000
RC$_2$	29	27	6.0×10^6	1000	6.0×10^6	1000

Table 9
Connection parameters of casing-base.

Connection	Casing (node)	k_{cx} (N/m)	k_{cy} (N m)	c_{cx} (N s/m)	c_{cy} (N s/m)
CB$_1$	6	7.5×10^6	5.0×10^7	2000	0
CB$_2$	26	7.5×10^6	5.0×10^7	2000	0

3.2.2. Modal experiment verification

In this study, modal experiments of the rig under the support state are conducted, and the frequency response functions are obtained by the slow sine scanning method. The main equipment used for this purpose include an NI9234 dynamic signal acquisition module (NI Corporation), a 4805-type ICP acceleration sensor (B&K Company), and a HEV-50A-type vibration exciter (Vibration Engineering Institute, Nanjing University of Aeronautics and Astronautics).

The modal experiment sketch map is shown in Fig. 9, and photographs of the experiment are shown in Figs. 10–12. Seven acceleration test points are installed on the rotor and casings; test points 2 and 6 are installed on the casings, and the other test points are installed on the rotor. Test point 1 is an excitation point as well, which is connected with the exciter, and a force sensor is installed between the exciter and the excitation point to measure the excitation force. The excitation force and response signals are collected by a computer, and the frequency response functions, which include $H_{11}(f)$, $H_{21}(f)$, $H_{31}(f)$, $H_{41}(f)$, $H_{51}(f)$, $H_{61}(f)$, and $H_{71}(f)$, can be obtained through signal processing and analysis.

In Fig. 13, the experiment and simulation amplitude frequency response functions $H_{11}(f)$, $H_{31}(f)$, $H_{51}(f)$, and $H_{71}(f)$ are compared. Here, the sine slow scanning method is used as the modal analysis method in the simulation and experiment. The first three orders of experimental modal shapes are shown in Fig. 14, and the first three orders of computation modal shapes are shown in Fig. 15. In Figs. 14 and 15, the first and second order shapes are rigid shapes, indicating that the rotor does not deform; the third shape is z bent shape. From Figs. 14 and 15, the simulation results agree well with the experimental values, proving that the proposed finite element rotor–support–casing coupling system dynamics model is correct and effective.
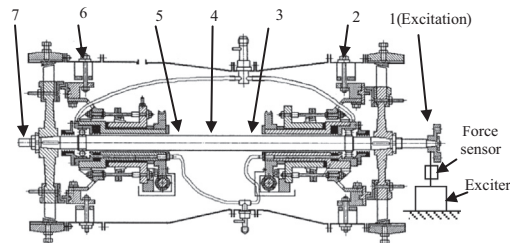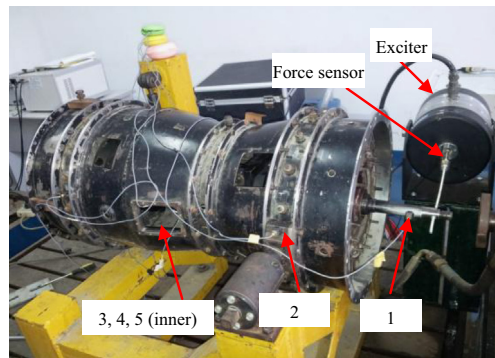

Fig. 9. Modal experiment sketch map.

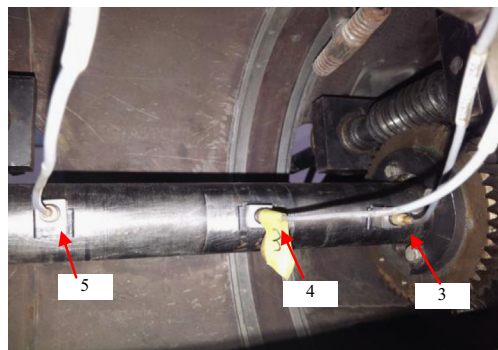**Fig. 10.** Test points' positions 1.
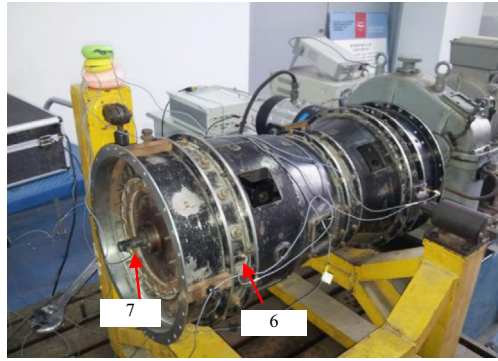

Fig. 11. Test points' positions 2.

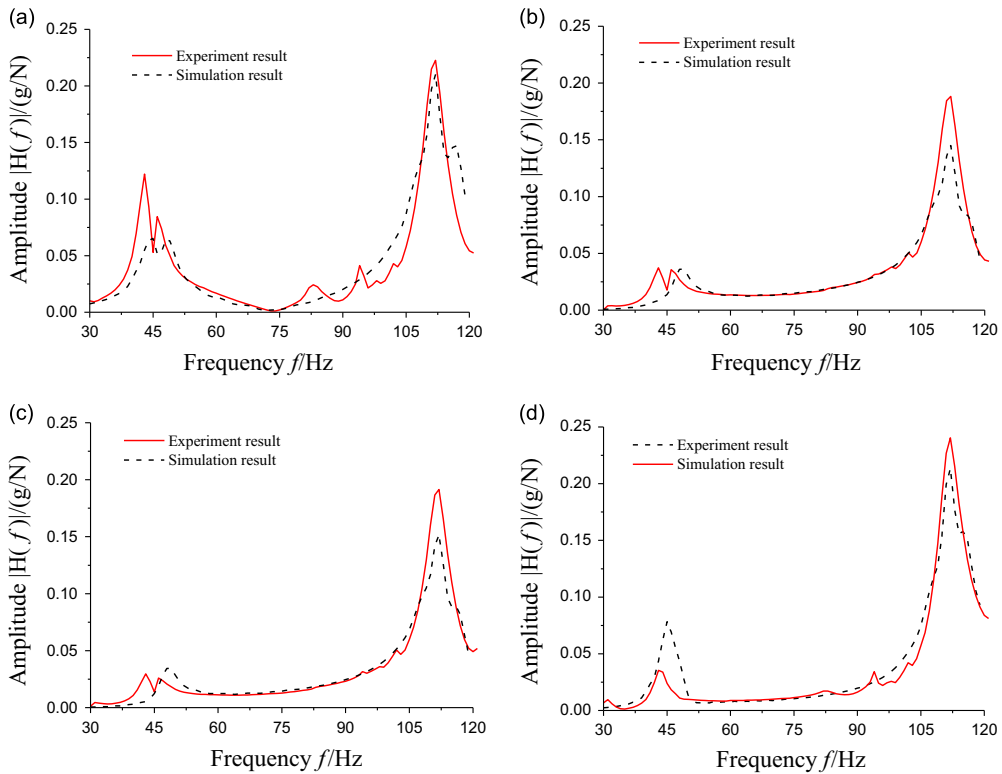**Fig. 12.** Test points' positions 3.

Fig. 13. Amplitude-frequency response function plots' contrast: (a) the test point 1; (b) the test point 3; (c) the test point 5; and (d) the test point 7.
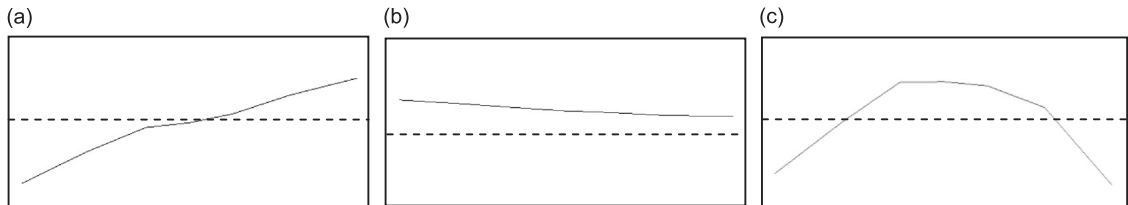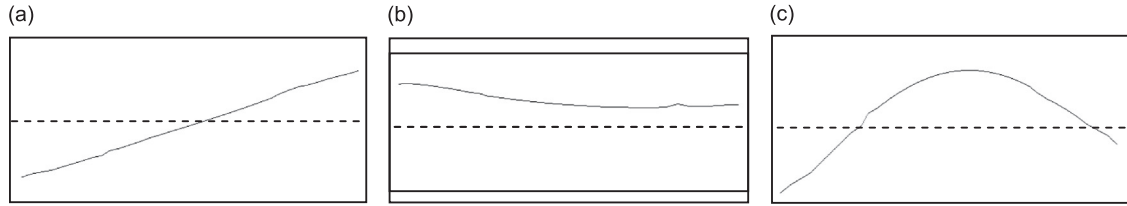

Fig. 14. First three orders' modal shapes in experiment results: (a) first order (43.4 Hz); (b) second order (46.5 Hz); and (c) third order (113.0 Hz).

4. Vibration fault simulation of certain types of missile turbofan engines

4.1. Aero-engine model and whole aero-engine vibration fault

Fig. 16 shows a structure sketch map of the rotor–ball-bearing–casing model for certain types of missile turbofan aero-engines, where P_1 denotes the fan disk; P_2, the motor disk; P_3, the compressor disk; P_4, the turbine disk; C_1, the intermediate

Fig. 15. First three orders' modal shapes in simulation results: (a) first order (44.5 Hz); (b) second order (48.4 Hz); and (c) third order (111.9 Hz).
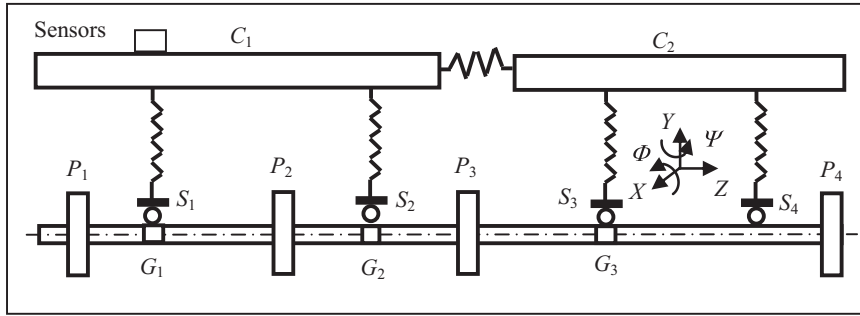
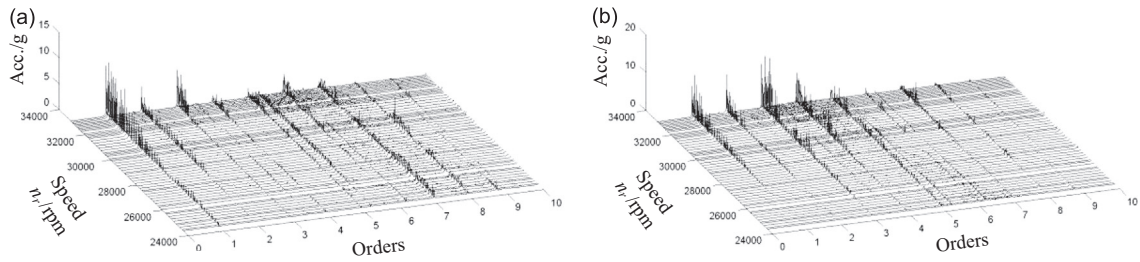**Fig. 16.** Sketch map of certain types of missile turbofan aero-engines.

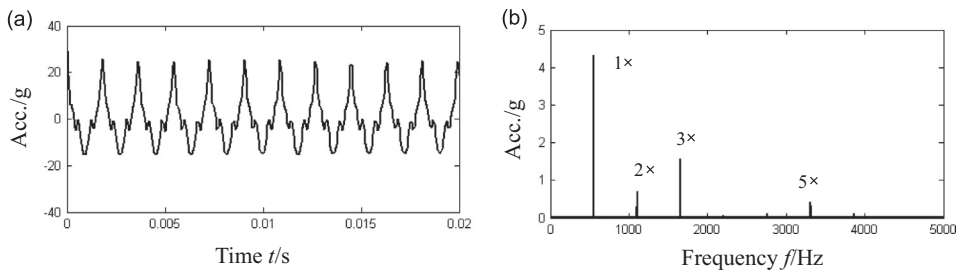**Fig. 17.** 3D waterfall plots: (a) lateral horizontal direction and (b) vertical direction.

Fig. 18. Horizontal acceleration signal at speed of 33,093 rpm: (a) waveform and (b) spectrum.

casing; C_2, the combustor casing; G_1, the gear coupling between the fan shaft and the transmission shaft; G_2, the gear coupling between the transmission shaft and the compressor shaft; G_3, the gear coupling between the compressor shaft and the turbine shaft; S_1, the fan support point bearings; S_2, the compressor front support bearings; S_3, the compressor rear support bearings; and S_4, the turbine support bearings.

The aero-engine's radial vibrations are measured by two acceleration sensors, one of which is installed on the aero-engine's lateral horizontal position and the other, on the aero-engine's top vertical position. The sampling frequency is 12.8 kHz.

During the trial running process, the whole aero-engine vibration value often exceeds the standard limit. The 3D waterfall plots of certain trial running data obtained from the No. Z09077 aero-engine are shown in Fig. 17. Fig. 17 shows that the vibration appears abnormal at high speeds and that there are many multiple-frequency components. The experimental data at a speed of 33,093 rpm is selected for analysis. The waveforms and spectrums of the horizontal and vertical signals, which are denoised by the auto-correlation method, are shown in Figs. 18 and 19, respectively. From Fig. 18, the horizontal acceleration signal shows an obvious $1 \times$ component and $2 \times$ component, but the $2 \times$ component was
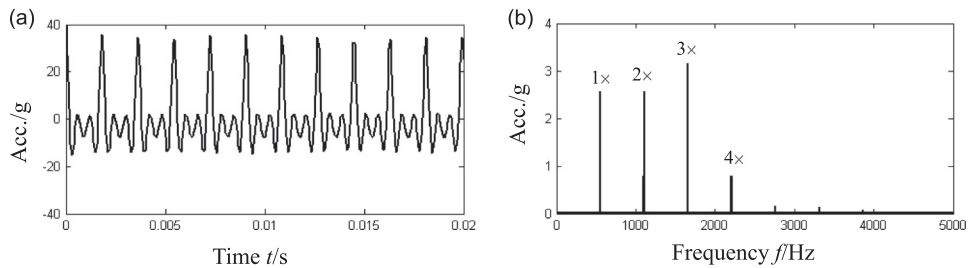
Fig. 19. Vertical acceleration signal at speed of 33,093 rpm: (a) waveform and (b) spectrum.
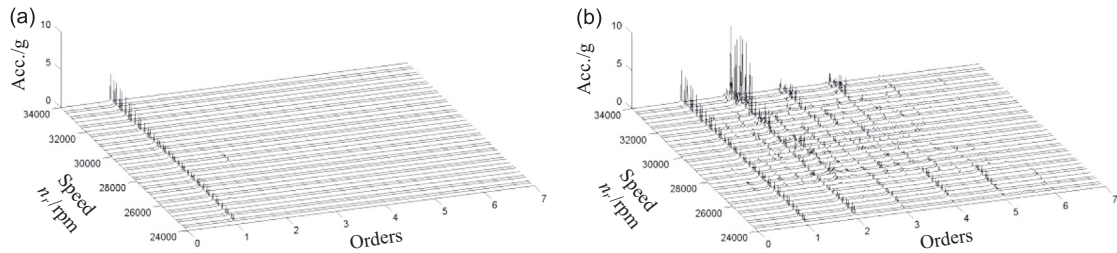

Fig. 20. 3D waterfall plots of vibration acceleration signals in horizontal direction: (a) normal and (b) looseness fault.

relatively weak. From Fig. 19, in the vertical acceleration signal, the $2\times$ component and $3\times$ component are basically the same as the $1\times$ component. The waveforms show a typical shock characteristic, with a truncated shape and longitudinal asymmetricity.

According to an exchange with the trial running staff, it can be initially estimated that the fault for whole aero-engine vibration may be caused by the looseness of the bearing housing. Therefore, in this study, fault simulations for the whole aero-engine were performed using the established vibration modelling for a whole aero-engine by considering the looseness fault. The simulation results were compared with the trial running signals to determine the mechanism of aero-engine vibration.

4.2. Simulation of looseness fault

To simulate the aero-engine's looseness fault, first, the rotor unbalance excitations are considered, in which the eccentricities of the fan disk, motor disk, compressor disk, turbine disk 1, and turbine disk 2 are all set as 0.01 mm. Then, the looseness fault of the bearing housing is modelled. Assume that the equivalent stiffness between the bearing housing and the casing is k_{f0} and looseness amount of the bearing housing is δ considering the segmentation linearization under the condition of relative displacement of bearing housing and casing. Then, the segmentation stiffness k_f is

$$k_f = \begin{cases} k_{f0} & (x_b - x_c > \delta) \\ k_{f0}/5 & (0 \le x_b - x_c \le \delta) \\ 5k_{f0} & (x_b - x_c < 0) \end{cases} \tag{12}$$

where x_b represents the displacement of the bearing housing and x_c, the displacement of the casing. The calculation formulas for the horizontal and vertical directions are the same.

In this study, the looseness faults at the fan support point S_1 are considered. The horizontal and vertical looseness between the bearing housing and the casing are set together, and their looseness amounts are all 1.0 μm.

Fig. 20 shows the simulation results for speeds of 24,000–35,000 rpm. Fig. 20(a) shows the simulation result under normal conditions, and (b) shows the simulation result for the looseness fault. Fig. 20 shows that a looseness fault leads to a vibration increase, and that with an increase in rotating speed, the imbalance forces increase rapidly such that the looseness faults are fully excited, and many multiple-frequency components appear. Figs. 21 and 22 show the waveforms and spectrums of the casing horizontal acceleration signals that are denoised by the auto correlation method. From the figures, the vibration signals have obvious multiple-frequency components, such as $2\times$, $3\times$, $4\times$, and $5\times$, and these components' amplitudes are basically the same as or exceed those of the $1\times$ component. In addition, the waveforms also show a typical shock characteristic, with a truncated shape and longitudinal asymmetricity.

It can be found out that the pseudo-resonance of the system would have been noted at 32,350 rpm in Fig. 22(b), and it has a dominant frequency of $2\times$ rotor speed; therefore, it can be inferred that it is appropriately characterised as the 2nd-order super-harmonic of a system having a fundamental critical speed of $2 \times 32{,}350$ rpm or 64,700 rpm. The other pseudo-resonance of the system, identified in Fig. 21, occurs at a speed of 25,900 rpm, which appears to be precisely 0.400 or
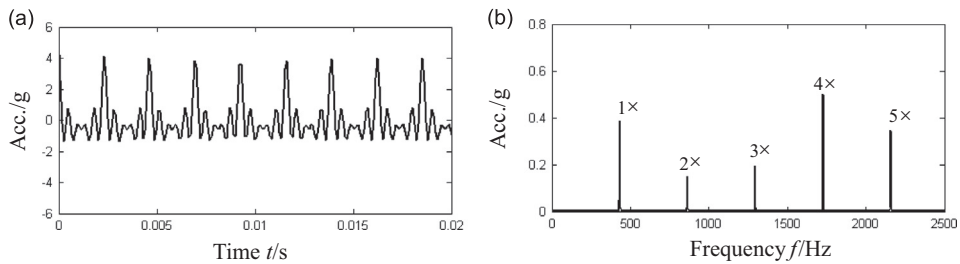
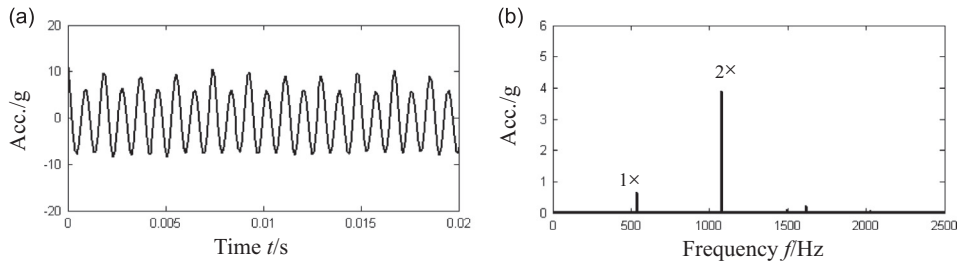**Fig. 21.** Horizontal acceleration signal at speed of 25,900 rpm: (a) waveform and (b) spectrum.

Fig. 22. Horizontal acceleration signal at speed of 32,350 rpm: (a) waveform and (b) spectrum.
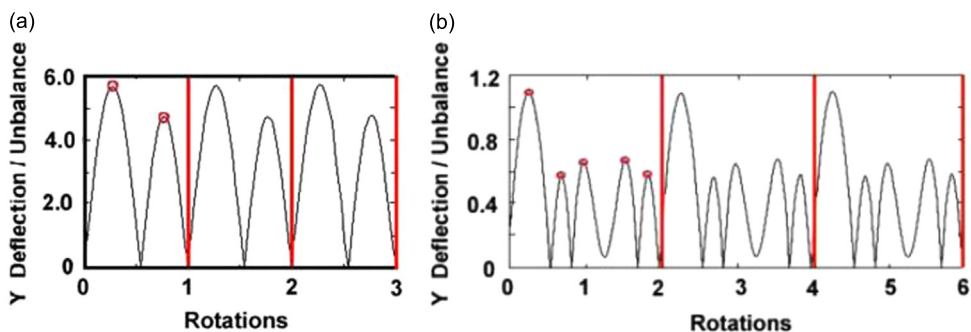

Fig. 23. Waveform of pseudo-resonance obtained by Ehrich's model in the literature [14]: (a) waveform of pseudo-resonance at one-half of the system's critical speed and (b) waveform of pseudo-resonance at two-fifth of the system's critical speed.

two-fifth of the fundamental critical speed. As shown in Fig. 23, such pseudo-resonances were also obtained by Ehrich's model in the literature [14], which involved a single-mass/single-degree of freedom connected by a single nonlinear (that is, bilinear) spring and a linear damper to ground. The comparisons between Figs. 22(a) and 23(a) and between Figs. 21(a) and 23(b) show the very good agreement of the waveforms generated in Ehrich's model and the proposed model.

4.3. Fault analysis

From a comparison between the experiment and the simulation results, it can be found that the looseness fault is easily excited at high speeds because of the great imbalance force, and when considering the looseness fault, the time waveform of the vibration acceleration of the casing exhibits a typical shock characteristic with a truncated shape and longitudinal asymmetricity; furthermore, there are many obvious multiple-frequency components in the spectrum.

Through the comparison analysis, excellent qualitative consistency is found between the simulation results and the experimental results. Therefore, it can be shown that the main fault in this aero-engine is connection looseness between the bearing housing and the casing.

It should be noted that an actual aero-engine structure is very complex and it is very difficult to completely simulate its dynamic behaviours; therefore, in this study, the fault simulation of the actual aero-engine can only simulate the fault characteristics in the time domain and frequency domain, and it is difficult to quantitatively simulate the dynamics behaviours.

5. Conclusions

(1) To investigate whole aero-engine vibration, a new coupling dynamic model for a whole aero-engine is established. In this coupling system, the rotor and casing systems are modelled using the finite element method. The shear deformations and inertias of the rotor and casing finite element unit are considered. The gyroscopic moments of the rotors are included. The nonlinear factors of the ball bearings are also considered. The numerical integration in the time domain, which combines the Newmark-β method and the Zhai method, is used to obtain the system's dynamic responses.

(2) In this study, four types of connection forms are defined: support connection between rotor and casing, coupling connection between rotors, elastic connection between casings, and installation connection between casing and base. By synthetically using these connections, the whole aero-engine with multiple rotors and casings can be modelled very conveniently.

(3) For a practical rotor–ball-bearing rig and rotor–ball-bearing–casing fault tester, a rotor–support coupling dynamic model and rotor–support–casing coupling dynamic model are established. The rotor tester is used for modal experiments, and good consistencies are found between the calculation results and the experimental results. Therefore, the results show that the proposed model is correct and effective.

(4) The vibration model for a certain type of missile turbofan whole aero-engine is established. Vibration responses including looseness fault are simulated; and the simulation results and real trial running vibration signals show good consistency, which is revealed by the mechanism of the aero-engine vibration fault.

References

[1] Editorial Board of Aero-engine Design Manual, *Aero-engine Design Manual (19th Part): Rotor Dynamics and Whole Machine Vibration*, Aerospace Industry Press, Beijing, 2000, 208–226 (in Chinese).
[2] Y.X. Ou, P. Li, Mode synthesis analysis of vibration of entire engine, *Journal of Aerospace Power* 2 (3) (2007) 209–214. (in Chinese).
[3] M. Chen, Y.H. Ma, S.G. Liu, J. Hong, Rotor dynamic analysis of whole aero-engine models based on finite element method, *Journal of Beijing University of Aeronautics and Astronautics* 33 (9) (2007) 1013–1016. (in Chinese).
[4] J. Hong, H. Wang, D.W. Xiao, M. Chen, Effects of dynamic stiffness of rotor bearing on rotordynamic characteristics, *Aeroengine* 4 (1) (2008) 23–27. (in Chinese).
[5] H.W. Chiang, C.N. Hsu, S.H. Tu, Rotor-bearing analysis for turbomachinery single- and dual-rotor systems, *Journal of Propulsion and Power* 20 (6) (2004) 1096–1104.
[6] G. Sun, A. Palazzolo, A. Provenza, C. Lawrence, K. Carney, An effective algorithm for blade loss simulations using a high fidelity ball bearing and damper model, *Proceedings of the American Society of Mechanical Engineering 19th Biennial Conference on Mechanical Vibration and Noise*, Chicago, USA, September 2003, DETC 2003/VIB 48424.
[7] G. Sun, A. Palazzolo, A. Provenza, C. Lawrence, K. Carney, Long duration blade loss simulations including thermal growths dual-rotor gas turbine engine, *Journal of Sound and Vibration* 316 (2008) 147–163.
[8] P.M. Hai, P. Bonello, An impulsive receptance technique for the time domain computation of the vibration of a whole aero-engine model with nonlinear bearings, *Journal of Sound and Vibration* 318 (2008) 592–605.
[9] G. Chen, A new rotor–ball bearing–stator coupling dynamic model for whole aero-engine vibration, *Journal of Vibration and Acoustics* 131 (6) (2009) 061009-1–061009-9.
[10] F.F. Ehrich, *Handbook of Rotordynamics*, Krieger Publishing Co., Malabar, FL, 2004.
[11] G. Chen, C.G. Li, D.Y. Wang, Nonlinear dynamic analysis and experiment verification of rotor–ball bearings–support–stator coupling system for aero-engine with rubbing coupling faults, *Journal of Engineering for Gas Turbines and power* 132 (2010) 022501-1–022501-9.
[12] G. Chen, Study on Nonlinear dynamic response of an unbalanced rotor supported on ball bearing, *Journal of Vibration and Acoustics* 131 (6) (2009) 061001-1–061001-9.
[13] W.M. Zhai, Two simple fast integration methods for large-scale dynamic problems in engineering, *International Journal for Numerical Methods in Engineering* 39 (24) (1996) 4199–4214.
[14] F.F. Ehrich, A new class of asynchronous rotordynamic response in high speed rotors, ASME Paper DETC2007/VIB-35912, New York, NY.

G. Chen is a Professor at the College of Civil Aviation, Nanjing University of Aeronautics and Astronautics, Nanjing, PR China. He is currently mainly engaged in whole aero-engine vibration, rotor-bearing dynamics, rotating machine fault diagnosis, pattern recognition and machine learning, signal analysis, and processing.